


Article

Boosting Piezocatalytic Performance of BaTiO₃ by Tuning Defects at Room Temperature

Donghui An ^{1,2,†}, Renhong Liang ^{1,2,†}, Hua Liu ¹, Chao Zhou ¹, Mao Ye ¹, Renkui Zheng ^{1,2}, Han Li ^{1,*} and Shanming Ke ^{1,2,*} 

¹ School of Physics and Materials Science, Guangzhou University, Guangzhou 510006, China; 355700210015@email.ncu.edu.cn (D.A.); nculrh@163.com (R.L.); lh245711@gzhu.edu.cn (H.L.); 2112319083@gzhu.edu.cn (C.Z.); yem001@gzhu.edu.cn (M.Y.); zrk@gzhu.edu.cn (R.Z.)

² School of Physics and Materials Science, Nanchang University, Nanchang 330031, China

* Correspondence: lihan@gzhu.edu.cn (H.L.); ksm@gzhu.edu.cn (S.K.)

† These authors contributed equally to this work.

Abstract: Defect engineering constitutes a widely-employed method of adjusting the electronic structure and properties of oxide materials. However, controlling defects at room temperature remains a significant challenge due to the considerable thermal stability of oxide materials. In this work, a facile room-temperature lithium reduction strategy is utilized to implant oxide defects into perovskite BaTiO₃ (BTO) nanoparticles to enhance piezocatalytic properties. As a potential application, the piezocatalytic performance of defective BTO is examined. The reaction rate constant increases up to 0.1721 min⁻¹, representing an approximate fourfold enhancement over pristine BTO. The effect of oxygen vacancies on piezocatalytic performance is discussed in detail. This work gives us a deeper understanding of vibration catalysis and provides a promising strategy for designing efficient multi-field catalytic systems in the future.

Keywords: piezocatalysis; oxygen vacancies; room temperature lithium reduction; ultrasonic cavitation; multi-field catalysis



Citation: An, D.; Liang, R.; Liu, H.; Zhou, C.; Ye, M.; Zheng, R.; Li, H.; Ke, S. Boosting Piezocatalytic Performance of BaTiO₃ by Tuning Defects at Room Temperature. *Nanomaterials* **2024**, *14*, 276. <https://doi.org/10.3390/nano14030276>

Academic Editor: Candida Milone

Received: 5 December 2023

Revised: 28 December 2023

Accepted: 20 January 2024

Published: 29 January 2024



Copyright: © 2024 by the authors. Licensee MDPI, Basel, Switzerland. This article is an open access article distributed under the terms and conditions of the Creative Commons Attribution (CC BY) license (<https://creativecommons.org/licenses/by/4.0/>).

1. Introduction

With the development of industrialization and urbanization, the pollution of water resources by organic pollutants has caused severe environmental problems. This issue even threatens human health and life [1,2]. Therefore, it is imperative to address wastewater treatment and enhance the ecological environment. Recently, piezocatalysis has gained significant attention due to its ability to degrade organic pollutants and purify water through the abundant mechanical vibration in nature [3–7]. During a typical piezocatalysis process, electron and hole pairs are generated on the surface of the piezoelectric material under mechanical stress and separated by the piezoelectric potential. Subsequently, a series of oxidation/reduction reactions occur to produce reactive radicals to decompose the dye molecules [8,9]. Many piezoelectric materials, such as BaTiO₃ [10–13], ZnO [14], KNbO₃ [15], BaSrTiO₃ [16], and ZnSnO₃ [17], have been extensively investigated as efficient catalysts for the degradation of organic pollutants and water splitting. However, compared with the catalytic performance of electrocatalysis and photocatalysis, the catalytic activity of these piezoelectric materials is currently unsatisfactory, which limits their practical applications [18,19]. Therefore, there is an urgent need to develop novel strategies to enhance their catalytic activity [20–23]. As the piezoelectric effect solely contributes to the charge separation rather than the excitation of electron–hole pairs, the carrier concentration plays a crucial role in enhancing piezocatalytic performance [3–9]. Oxygen vacancies are commonly occurring defects in oxides and can be utilized to modulate the carrier concentrations [24,25]. Recently, Wang et al. [17] reported a hydrogen reduction approach used to generate surface defects in ZnSnO₃ nanowires, which demonstrated remarkable

piezocatalytic activity through capitalizing on well-modulated oxygen vacancies. Barium titanate nanoribbons with defects exhibit improved piezocatalytic performance owing to their increased carrier concentrations derived from oxygen vacancies [26]. These findings suggest that the modulation of oxygen vacancies represents a viable and crucial approach for improving the piezocatalytic activity of piezoelectric oxides [27,28].

So far, the generation of oxygen vacancies in piezocatalysts has mainly been achieved through heating treatment under vacuum [26,29] or hydrogen atmosphere [30,31]. However, these methods have limitations, such as harsh reaction conditions (e.g., high temperature and pressure) and complex synthesis procedures. Therefore, there is a need for an efficient and scalable synthesis method for piezocatalysts with controlled oxygen concentration at room temperature, along with the optimization of their piezocatalytic activities for practical applications. In this regard, Ou and co-workers proposed a simple approach for the synthesis of black TiO₂ using a lithium reduction method [32]. The lithium reduction strategy offers several advantages, including all-room-temperature processing, controllability, time efficiency, versatility, and scalability. It is reasonable to expect that the lithium reduction method could also be an effective approach for modulating oxygen vacancies in piezoelectric oxides.

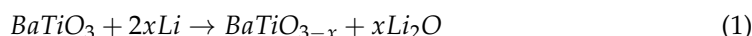
In this study, the effect of lithium reduction on the piezocatalytic performance of BaTiO₃ (BTO) nanoparticles was investigated. BTO nanoparticles with varying concentrations of oxygen vacancy were obtained by grinding raw powders with different proportions of lithium powders at room temperature. The oxygen vacancies were characterized using scanning transmission electron microscopy, and the piezoelectric response of the samples was demonstrated by piezoresponse force microscopy. The optimized piezocatalysts exhibited a degradation efficiency of up to 97% within a 20 min timeframe. We propose a mechanism for ultrasonic vibration-driven piezocatalysis and provide a comprehensive understanding of the influence of oxygen vacancies on the synergistic coupling effect of piezocatalysis and ultrasonic cavitation.

2. Materials and Methods

2.1. Preparation of Catalysts

The used raw materials are commercially available Barium titanate nanopowders (BaTiO₃, 99.9% metals basis, <100 nm), passivated Li powders (99.9%), and dimethyl carbonate (DMC, 99.95%). All reagents were directly used without further purification.

In this study, 5 g of Barium titanate (BTO) and a specific proportion of passivated lithium powder were weighed and placed into a mortar for grinding. To ensure thorough grinding, an appropriate amount of dimethyl carbonate (DMC) was added as a dispersant. The grinding process was conducted in a glove box filled with Ar gas to prevent oxidation of the lithium powder by air. After grinding for one hour, the sample was removed from the mortar and washed with dilute hydrochloric acid (HCl) to dissolve the lithium oxide generated during the reduction process. The sample was then subjected to centrifugation and washed three times with deionized water. The resulting sample was denoted as BTO-*x* (*x* wt% = 0 wt%, 1 wt%, 3 wt%, 5 wt%, 7 wt%, and 10 wt%, where *x* represents the weight percentage (wt%) of lithium powder used in the reduction process). By adjusting the ratio of lithium metal powder, the defect content in the BTO nanoparticles was controlled. The reduction process occurred spontaneously at room temperature, as indicated in Equation (1).



2.2. Characterization

An X-ray diffractometer (SmartLab, Rigaku, Tokyo, Japan) was used to investigate the phase structure of the BaTiO₃ samples. The absorbance and diffuse reflectance properties were examined using a UV-Vis spectrophotometer (UH4150, HITACHI, Tokyo, Japan). Raman spectra were collected at room temperature using a confocal microscope spec-

trometer (WITec Alpha300 Raman, Ulm, Germany) with a 532 nm laser source. A probe aberration-corrected STEM microscope [FEI Titan 80–300 (Hillsboro, OR, USA) operating at 300 kV and JEOL JEM-ARM200CF (Tokyo, Japan) operating at 200 kV] was utilized. X-ray photoelectron spectroscopy (XPS) was performed using a Thermo Fischer (Waltham, MA, USA), ESCALAB Xi+ instrument. High-resolution transmission electron microscopy (HRTEM), energy-dispersive X-ray spectroscopy (EDS), STEM high-angle annular dark-field (HAADF) observation, and electron energy loss spectroscopy (EELS) were conducted on an FEI Titan 80–300 microscope to probe the structural and chemical evolution of samples. Atomic force microscopy (Cypher ES, Oxford, Santa Barbara, CA, USA) coupled with piezoelectric reaction force microscopy (PFM) was employed to perform piezoelectric reaction measurements on the prepared samples. Photoluminescence (PL) measurements were carried out using an FLS900 fluorimeter (Edinburgh Instruments, Livingston, UK). Electrochemical impedance spectra (EIS) were obtained using the CHI660E electrochemical analyzer (Chenhua, Shanghai, China). Electron paramagnetic resonance (EPR) spectra were recorded by a Bruker A300 (Freiberg, Germany) paramagnetic resonance spectrometer at room temperature.

2.3. Piezocatalytic Activity Experiments

The piezocatalytic activities of the BTO-*x* samples were evaluated by decomposing Rhodamine B (RhB) with an ultrasonic cleaner (150 W and 40 kHz). Representatively, 0.05 g of the BTO-*x* powders was dispersed into 50 mL of RhB solution (5 mg/L). The mixed solution was stirred in the dark for 30 min to allow for adsorption and desorption equilibrium before ultrasonic irradiation to balance adsorption-desorption. Then, a 50 mL glass beaker containing the mixed suspension was fixed in a specific position within an ultrasonic cleaner. To monitor the degradation process, 3 mL of the clarified solution was sampled every 5 min and subjected to centrifugation to segregate the BTO-*x* powders. The concentration of the dye in the aqueous solution was determined using a UV-Vis spectrophotometer. The regularity of the degradation process was confirmed by repeating the experiments under the same conditions. In addition, the synergistic catalytic activity of barium titanate samples under ultraviolet (UV) was evaluated using an ultraviolet (125 W, 365 nm) light source. Furthermore, the degradation experiments were repeated using recovered BTO-5 to evaluate the cycling stability of the piezoelectric catalyst for RhB degradation.

3. Results

Figure 1a provides a schematic representation of the lithium reduction treatment and piezocatalytic processes of the BaTiO₃ nanoparticles. The X-ray diffraction (XRD) patterns of the BTO-*x* samples, as shown in Figure 1b, exhibit a good match with pseudo-cubic BTO (PDF#89-2475). The diffraction peaks of all samples demonstrate the high crystallinity and purity of BTO, without any impurity such as Li₂O. This indicates that the intrinsic crystal structure of the barium titanate nanoparticles remains unchanged after the lithium reduction process. However, there is a gradual shift of the main diffraction peak to a higher angle with increasing Li content, indicating the implantation of oxygen vacancies into the BTO nanoparticles and an expansion of the unit cell. The expansion of the lattice due to the presence of oxygen vacancies is a well-known phenomenon observed in oxide materials. Oxygen vacancies typically cause an overall expansion of the oxide lattice on both short- and long-range scales [33,34]. The room-temperature Raman vibrational spectroscopy experiments were conducted to examine the local distortions of the lattice and confirm the crystal structures. Figure 1c shows the Raman spectra of all the analyzed samples. The characteristic peaks centered around 306, 516 and 716 cm⁻¹ could be assigned to the B1, E(TO+LO); E, A1(TO); and E, A1(LO) modes, respectively. These peaks indicate the presence of an acentric structure resulting from structural disorder of the Ti⁴⁺ ions within the [TiO₆] octahedra [35–38]. It is well known that the ideal cubic BTO is Raman inactive due to the isotropic distribution of electrostatic forces around the Ti⁴⁺ ions within each

octahedron [39]. However, the presence of tetrahedral distortion of $[\text{TiO}_6]$ octahedra can induce piezoelectric effects, even though the X-ray diffraction patterns of BTO suggest a global cubic-like symmetry [40–42].

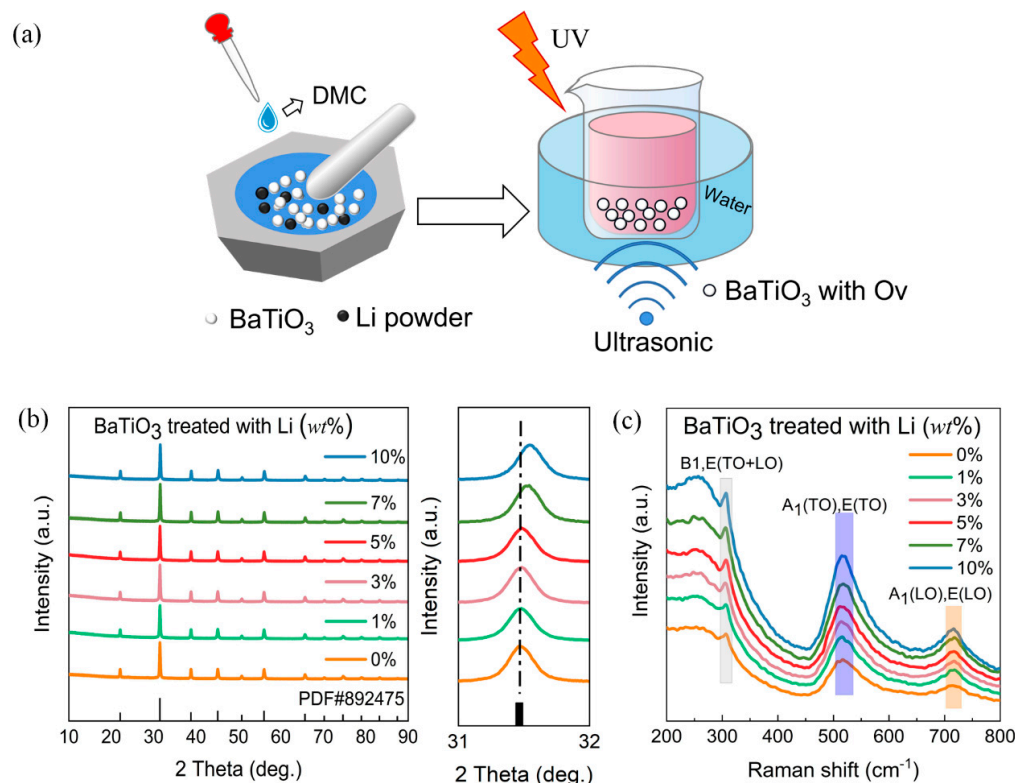


Figure 1. (a) The schematic of lithium reduction treatment and piezocatalytic test. (b) XRD patterns and the selected diffraction peak near 31.5° of the BTO-x samples. (c) Room-temperature Raman spectra of the BTO-x samples.

In Figure S1, scanning electron microscope (SEM) images reveal that the particle size of the BTO samples remains almost the same before and after the lithium reduction treatment. Additionally, the surface morphology of BTO is not altered after grinding with lithium powders. To further examine the detailed morphology and microstructure of BTO-5, aberration-corrected scanning transmission electron microscopy (STEM) was employed. As shown in Figure 2a, BTO-5 displays a crystalline-disordered core-shell structure. A distinct disordered layer with a thickness of approximately 1 nm is clearly visible in the STEM image. The elemental map of oxygen obtained through energy-dispersive X-ray spectroscopy (EDS) (Figure 2b,c) reveals that the disordered layer has a lower oxygen content compared to the interior of the BTO particle. This indicates that oxygen vacancies have been introduced into the surface of the BTO as a result of the reduction of surface lattice oxygen by lithium at room temperature.

To further investigate the presence of oxygen vacancies in the surface layer of the BTO-5 sample, atomic-resolution electron energy loss spectroscopy (EELS) line-scanning was conducted from the surface to the bulk of the particle. Figure 2d displays a high-angle annular dark-field scanning transmission electron microscopy (HAADF-STEM) image with the EELS line-scan range indicated for a BTO-5 particle. Representative EELS spectra of the $\text{Ti-L}_{2,3}$ and O-K edges in three different regions, spanning from the surface to the bulk, are highlighted in Figure 2e. All spectra are normalized to the Ti L_2 peak. The Ti-L_3 and Ti-L_2 peaks exhibit a noticeable energy shift towards higher energy at the surface compared to the core region (Figure 2e,f). In addition, the intensity ratio of L_2/L_3 decreases from the surface to the inner part, indicating that the Ti oxidation state at the surface is lower than in the inner region. This suggests a reduction in the Ti^{4+} ions at the surface layer.

Furthermore, the intensity of the O-K edge peak is suppressed, indicating a decrease in the oxygen content at the surface. This suppression of the O-K edge peak is attributed to the formation of oxygen vacancies in the surface layer [43–47].

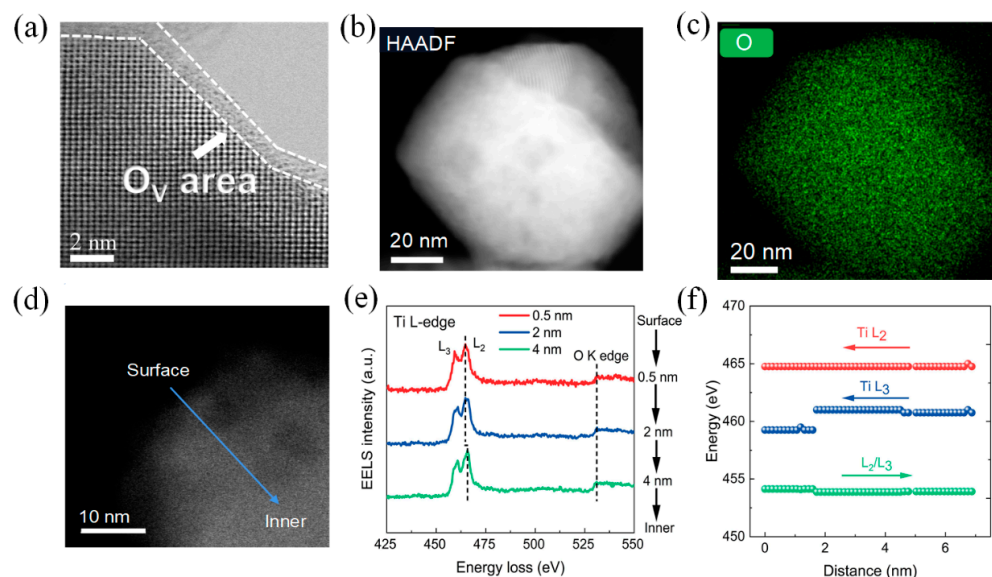


Figure 2. (a) BF-STEM image of a particle from the BTO-5 sample. (b) HAADF-STEM image of a particle from the BTO-5 sample. (c) the EDS elemental maps of O. (d) HAADF-STEM image of a particle from the BTO-5 sample with the EELS line-scan. (e) EELS spectra of the Ti- $L_{2,3}$ and O-K edges taken along the blue line in (d), where the black dotted lines show the main peaks of the Ti- $L_{2,3}$ and O-K edges. (f) Ti- L_3 and Ti- L_2 energy profiles and L_2/L_3 intensity ratio as a function of position.

The presence of oxygen vacancies can be further confirmed through X-ray photoelectron spectroscopy (XPS) and electron paramagnetic resonance spectroscopy (EPR) studies. Figure 3a shows the O 1s XPS spectra of the BTO- x samples. The O 2p peak at ~ 529.7 eV is attributed to the lattice oxygen, while the peak at ~ 530.8 eV corresponds to the signal of surface hydroxyl groups, indicating the presence of oxygen vacancies [48,49]. The percentage of O 1s peaks assigned to hydroxyl groups gradually increases from BTO-0 to BTO-10, indicating an increase in the concentration of oxygen vacancies. It is worth noting that the lithium-reduced BTO samples do not contain any detectable lithium element, as confirmed by the absence of a Li 1s spectrum (Figure S2). This suggests that the lithium oxide was completely removed during the acid treatment. Furthermore, the EPR signal of oxygen vacancy is clearly observed at $g = 2.002$ in the Li-treated BTO samples, indicating the presence of oxygen vacancies (Figure 3b).

The piezoelectric properties of BTO nanoparticles were characterized and confirmed using piezoresponse force microscopy (PFM). Figure 4 presents the topography image and piezoelectric response of the BTO-5 sample. A typical ferroelectric butterfly amplitude curve is observed, along with a well-defined 180° phase change hysteresis loop. These observations provide clear evidence of the piezoelectricity of the BTO-5 sample.

The piezocatalytic activities of the BTO- x samples were evaluated by degrading Rhodamine B (RhB) dye under ultrasonic vibration at a frequency of 40 kHz and a power of 150 W under dark conditions, as shown in Figure 5a–c. According to the first-order kinetics, the degradation efficiency rate constant k is obtained from the slope of the $\ln(C_0/C)$ -time diagram. In the absence of any vibration, there was negligible dye degradation, indicating the essential role of vibration in the process. When ultrasonic vibration was applied without any catalyst, RhB degradation occurred to some extent, which can be attributed to the ultrasonic cavitation effect [50]. For the BTO- x samples, the piezocatalytic activity exhibited a trend of initially increasing and then decreasing, with the peak observed at 5 wt% Li-treated BTO. BTO-5 demonstrated superior piezocatalytic activity, with a k value

of 0.1189 min^{-1} . It is worth noting that defects have multiple effects on piezocatalytic properties. By increasing the amount of lithium powder during the room temperature process, more oxygen vacancies can be created, resulting in a higher concentration of carriers on the BTO surface. The piezocatalytic performance is generally proportional to the defect content, as it enhances carrier concentration, oxygen adsorption, and active sites. However, excess defects can be detrimental to piezocatalytic activity. They can act as charge recombination sites and reduce the piezoelectric polarization [51–53], thus negatively impacting the overall performance. Therefore, there is an optimal defect concentration that maximizes the piezocatalytic activity, as observed in the peak performance of the 5 wt% Li-treated BTO sample.

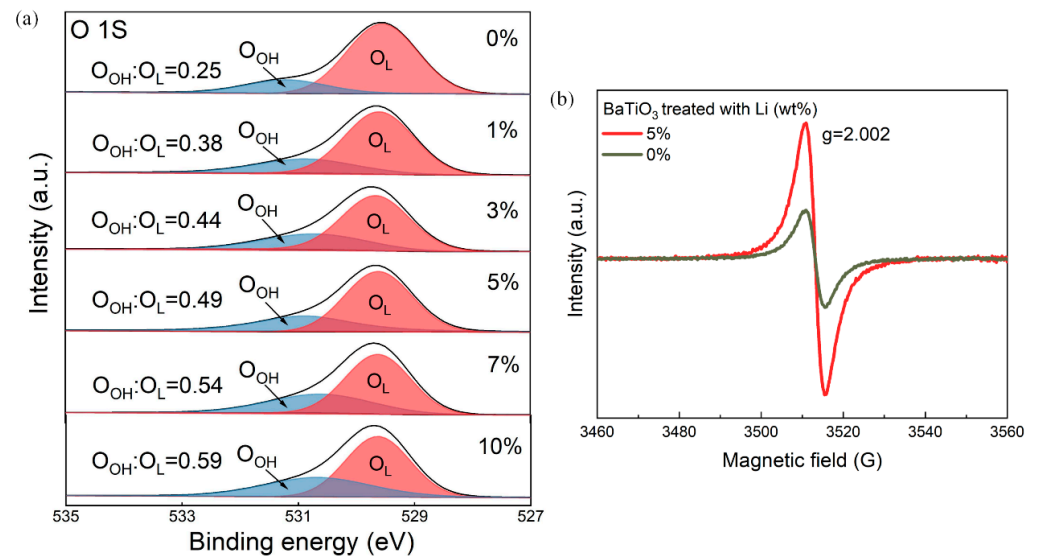


Figure 3. (a) O 1s XPS spectra of BTO-x samples. (b) EPR spectra of selected BTO-x samples.

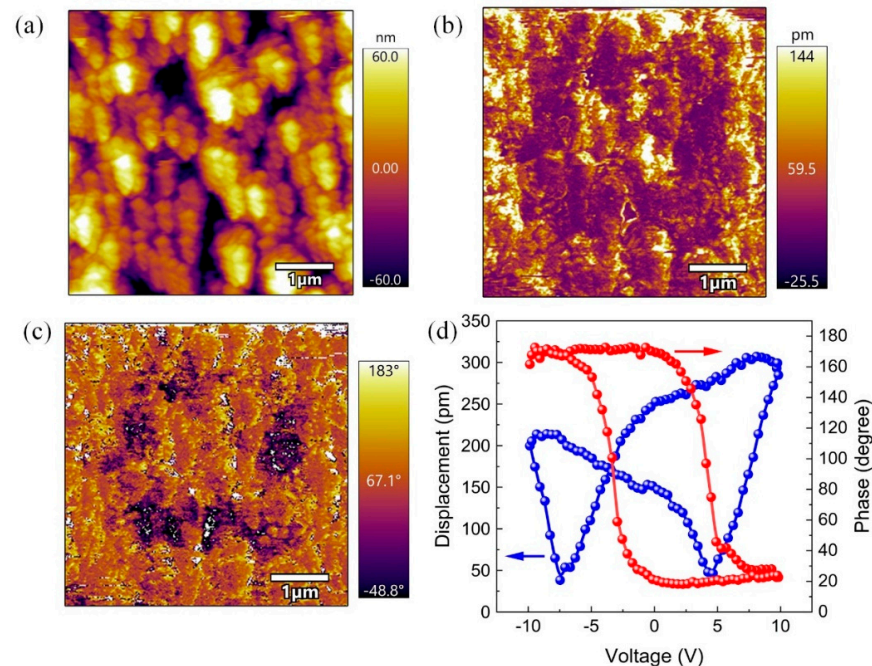


Figure 4. PFM results of BTO-5. (a) Topography image, (b) amplitude image, (c) phase image, and (d) the electric displacement and phase hysteresis loops.

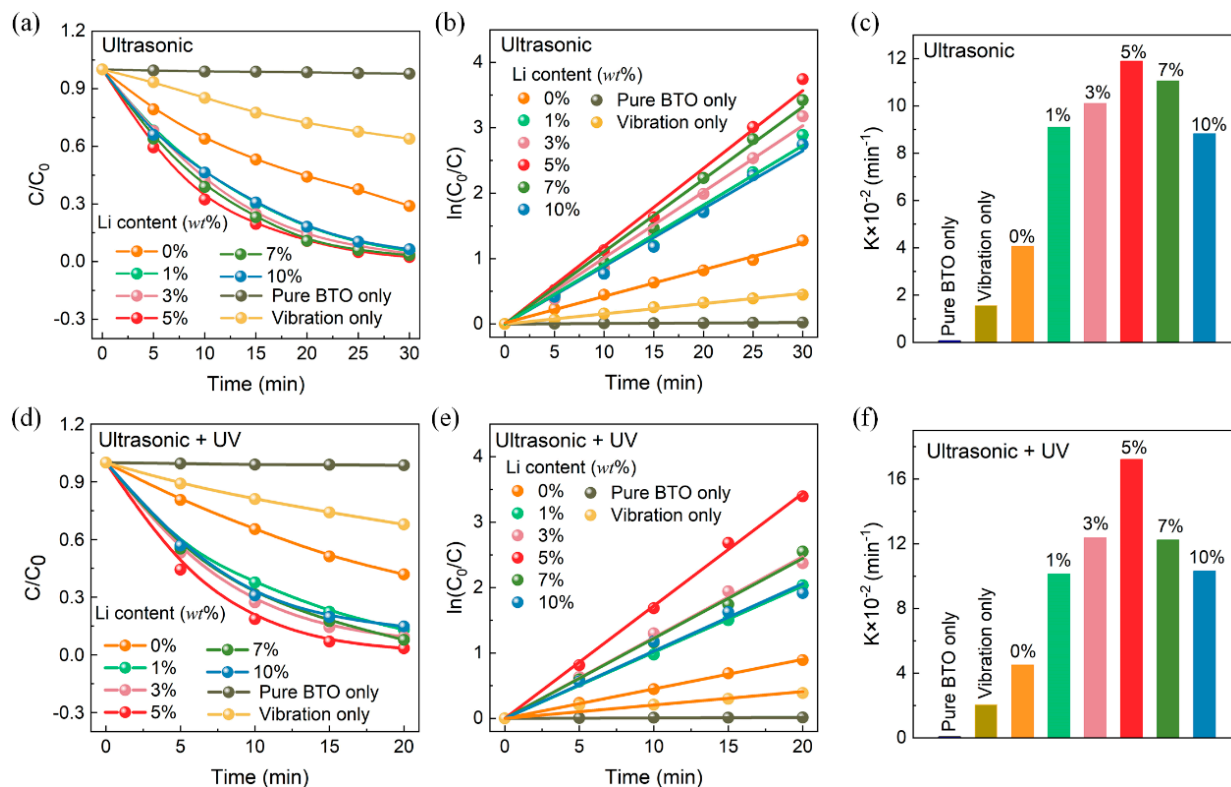


Figure 5. Effect of Li-treated BTO on the degradation of RhB. (a) The relative concentration ratios C/C_0 of RhB with different piezocatalysts and vibration state in the dark. (b) Plots of $\ln(C_0/C)$ versus the ultrasonic vibration time in the dark. (c) The corresponding reaction kinetics rate constant k values according to (b). (d) The C/C_0 of RhB under ultrasonic vibration and UV irradiation simultaneously. (e) Plots of $\ln(C_0/C)$ versus the ultrasonic vibration time under ultrasonic vibration and UV irradiation, and (f) the corresponding reaction kinetics rate constant k .

The influence of UV illumination alone on the experiments was explored, as shown in Figure S3. The results indicate that the photocatalytic performance of BTO nanoparticles is mediocre due to their large band gap (3.4 eV), regardless of the presence of oxygen vacancies. The absorption spectroscopy results in Figure S4 demonstrate that the band gap of BTO barely changes before or after Li treatment. The catalytic performance of BTO under the combined effect of UV irradiation and ultrasonic vibration is shown in Figure 5d–f. It was observed that the concentration of RhB decreased rapidly under the combination of UV irradiation and ultrasonic vibration. Among the BTO- x piezocatalysts, BTO-5 exhibited the highest reaction rate constant of 0.1721 min^{-1} , which is nearly four times that of pristine BTO. The k value is superior to that observed in other BTO-based experiments, listed in Table 1. Furthermore, the BTO- x piezocatalysts demonstrated favorable cyclic stability in terms of crystal structure, morphology, and piezocatalysis, as shown in Figure S5.

Table 1. Comparison of degradation efficiencies of various piezocatalysts.

Piezocatalyst	Dye Species	Vibration Source	Light Source	Initial Dye Concentration	Catalyst Dosage	Rate Constant	Ref.
BTO nanoparticles	RhB	150 W, 40 kHz	125 W, 365 nm	5 mg/L	1 g/L	0.1721 min^{-1}	This work
BTO nanoparticles	RhB	150 W, 40 kHz	dark	5 mg/L	1 g/L	0.1189 min^{-1}	This work
BTO nanobelts	RhB	100 W, 50 kHz	dark	10 mg/L	1 g/L	0.0253 min^{-1}	[26]
BTO nanosheets	MO	100 W, 40 kHz	/	5 mg/L	1 g/L	0.1279 min^{-1}	[54]
BTO nanowires	RhB	80 W,	/	5 mg/L	/	$<0.016 \text{ min}^{-1}$	[12]
BTO/TiO ₂ nanofibers	RhB	300 W, 40 kHz	250 W, 365 nm	5 mg/L	1 g/L	0.0967 min^{-1}	[10]
BTO nanofibers	RhB	100 W, 40 kHz	/	7.5 mg/L	1 g/L	0.0736 min^{-1}	[55]
ZnO/BTO heterostructures	RhB	120 W, 40 kHz	150 W	10 mg/L	1 g/L	0.118 min^{-1}	[56]

The effect of ultrasonic power on the catalytic performance was further investigated, taking into account the ultrasonic cavitation effect. Figure 6a–c illustrate the degradation of RhB under ultrasonic vibration (40 kHz, 75 W) in the dark. When the ultrasonic power was set at 150 W, the degradation rate of RhB by BTO-5 reached 98% within 30 min. However, when the ultrasonic power was halved to 75 W, the degradation rate decreased to 86% within the same time period. The reduction in ultrasonic energy not only weakens the ultrasonic cavitation effect but also reduces the stress and weakens the piezocatalytic effect. This leads to a suppression in the degradation efficiency of RhB.

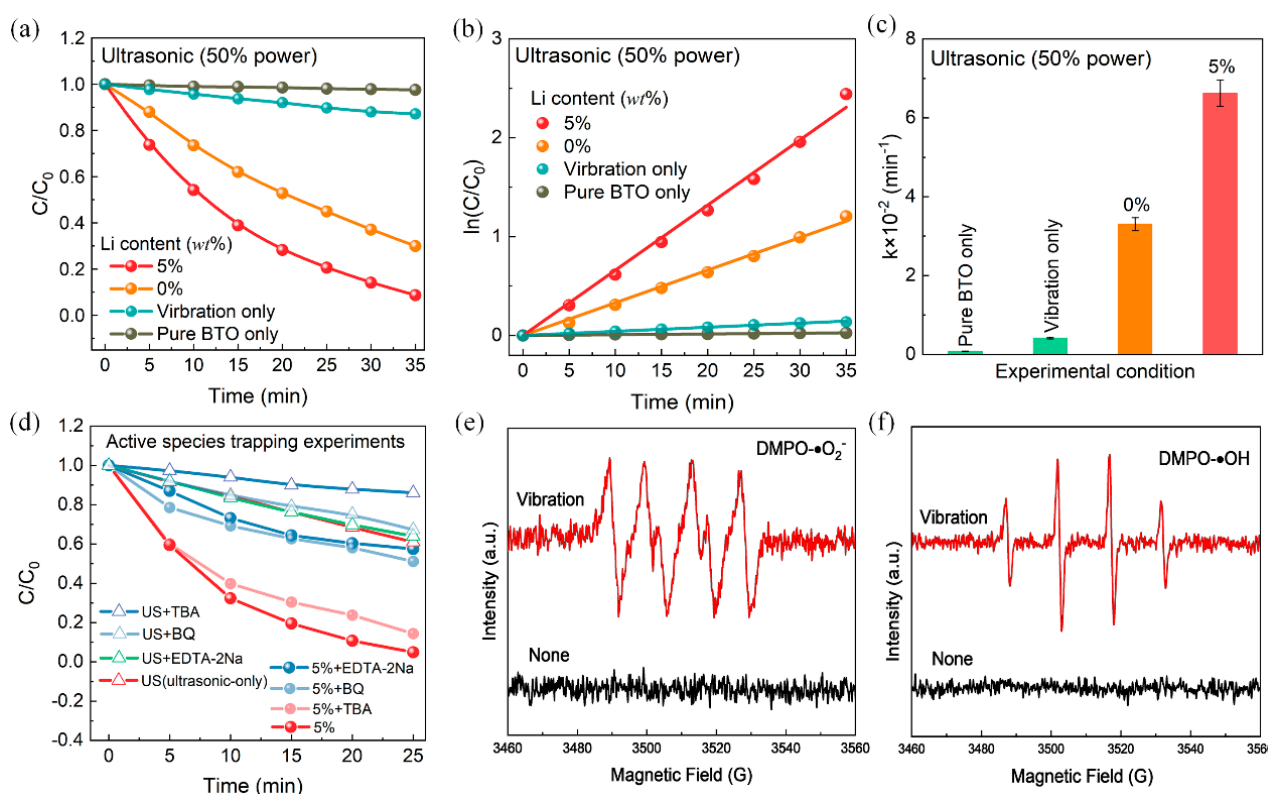


Figure 6. (a–c) Catalytic performance of BTO under ultrasonic vibration with a power of 75 W. (d) Active species trapping degradation experiments for catalysis system. (e) The ESR spectra of $\text{DMPO} \cdot \text{O}_2^-$ and (f) $\text{DMPO} \cdot \text{OH}$ using BTO-5 piezocatalyst.

4. Discussion

To investigate the role of active species in the ultrasonic vibration degradation of dyes, different scavengers (0.05 mmol) were used. Figure 6d compares the degradation efficiency with and without scavengers under ultrasonic vibration-only conditions. The addition of tert-butanol (TBA), an $\cdot\text{OH}$ scavenger, significantly reduced the degradation efficiency. This suggests that $\cdot\text{OH}$ radicals are the primary active species involved in the degradation of RhB molecules caused by the ultrasonic cavitation effect. It is well-known that $\cdot\text{OH}$ radicals can be generated from the dissociation of water molecules during the cavitation process induced by ultrasound [57]. On the other hand, the addition of benzoquinone (BQ, an $\cdot\text{O}_2^-$ scavenger) and ethylenediaminetetraacetate disodium (EDTA-2Na, a h^+ scavenger) only slightly decreased the degradation efficiency. This indicates that $\cdot\text{O}_2^-$ and h^+ radicals play a secondary role in the overall piezocatalytic degradation of RhB molecules. When BQ and EDTA-2Na were separately added to the piezocatalysis system, the degradation efficiency was significantly reduced, resulting in a degradation rate of only 50% for RhB within 25 min. This inhibitory effect can be attributed to the scavenging of $\cdot\text{O}_2^-$ and h^+ radicals, demonstrating that these species are the main active substances in the piezocatalytic degradation of RhB molecules. In addition, the active species were

confirmed via electron spin resonance (ESR). Figure 6e,f show the ESR spectra of DMPO- $\cdot\text{O}^{2-}$ and DMPO- $\cdot\text{OH}$, respectively. The DMPO- $\cdot\text{O}^{2-}$ spectra exhibited four groups of strong signals generated by ultrasonic vibrations, confirming the generation of $\cdot\text{O}^{2-}$ active species during the degradation process. Similarly, the ESR spectra of DMPO- $\cdot\text{OH}$ indicated the generation of $\cdot\text{OH}$ radicals. In conclusion, the results confirm that both $\cdot\text{O}^{2-}$ and $\cdot\text{OH}$ reactive species are generated during the degradation process. During the piezocatalytic process, the following chemical reactions are believed to occur:

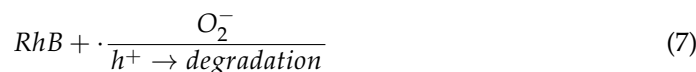
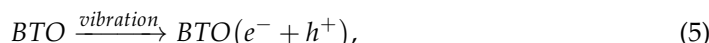
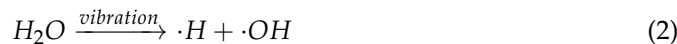


Figure 7a shows the photoluminescence (PL) spectra of pristine BTO and BTO-5. Both samples exhibit an emission peak at 713 nm when excited by 325 nm light. However, the fluorescence emission intensity of BTO-5 is slightly lower compared to pristine BTO. This decrease in intensity generally suggests that BTO-5 has less recombination of excited-state electron–hole pairs, leading to a longer carrier lifetime. Additionally, electrochemical impedance spectroscopy (EIS) was performed to evaluate the efficiency of electron–hole pair migration. As presented in Figure 7b, BTO-5 displays a smaller arc radius compared to pristine BTO. This indicates that the charge carriers in BTO-5 have improved emigration and transfer efficiencies due to the implanted defects. The smaller arc radius suggests that the charge carriers can move more easily and efficiently, enhancing the piezocatalytic activity of BTO-5. The combination of PL and EIS results confirmed that the oxygen vacancies in BTO play a crucial role in promoting effective charge carrier separation and facilitating their transfer. This improved charge carrier behavior contributes to the enhanced piezocatalytic activity of BTO-5.

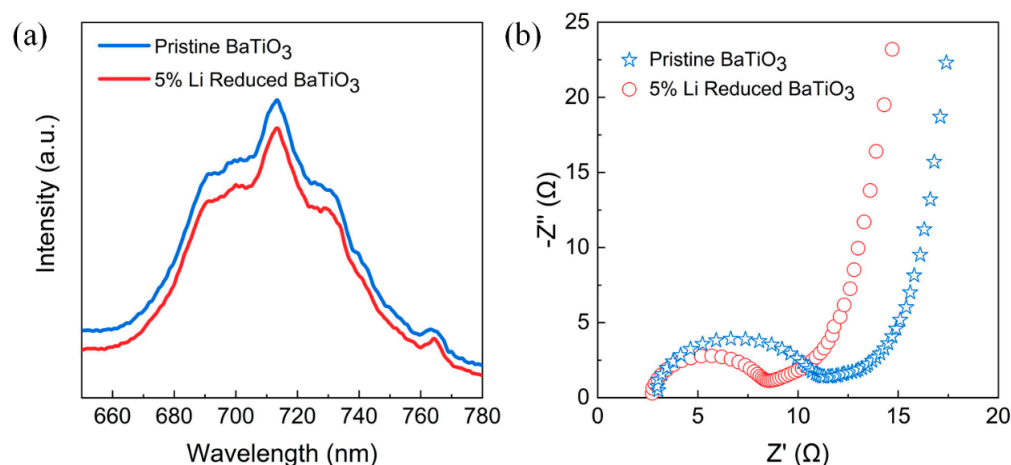


Figure 7. (a) Photoluminescence spectra and (b) the electrochemical impedance spectra of pure BTO and BTO-5, respectively.

In Figure 8, a schematic diagram illustrates the degradation of RhB through the synergistical piezocatalytic effect of BaTiO_3 with oxygen vacancies. The presence of free charge carriers plays a crucial role in the catalysis process. It is well known that oxygen vacancies in BTO create a shallow donor band near the conduction band, facilitating the

transition of photogenerated electrons from the valence band to the conduction band. This enhances the photocatalytic performance of BTO by increasing the concentration of free carriers. Furthermore, oxygen vacancies enhance the adsorption of O_2 , which is favorable for generating more hydroxyl groups through the ultrasonic cavitation effect [26]. The increased presence of hydroxyl groups, particularly $\cdot OH$ radicals, contributes to the degradation of RhB molecules. Oxygen vacancies also lead to a decrease in the elastic modulus of BTO [58]. Under the external stress generated by ultrasonic vibration, the “softer” BTO is more prone to bending, resulting in the generation of free carriers at a faster rate. In addition, BTO with oxygen vacancies exhibits higher surface conductivity, which is beneficial to the transmission of free carriers. Due to the piezoelectric polarization, a certain amount of positive and negative charges will be generated on the surface of the BTO, and an internal polarization electric field will be established. The internal polarization electric field can effectively attract the electrons and holes generated in the reaction to move in the opposite direction, thereby improving the catalytic performance of BTO.

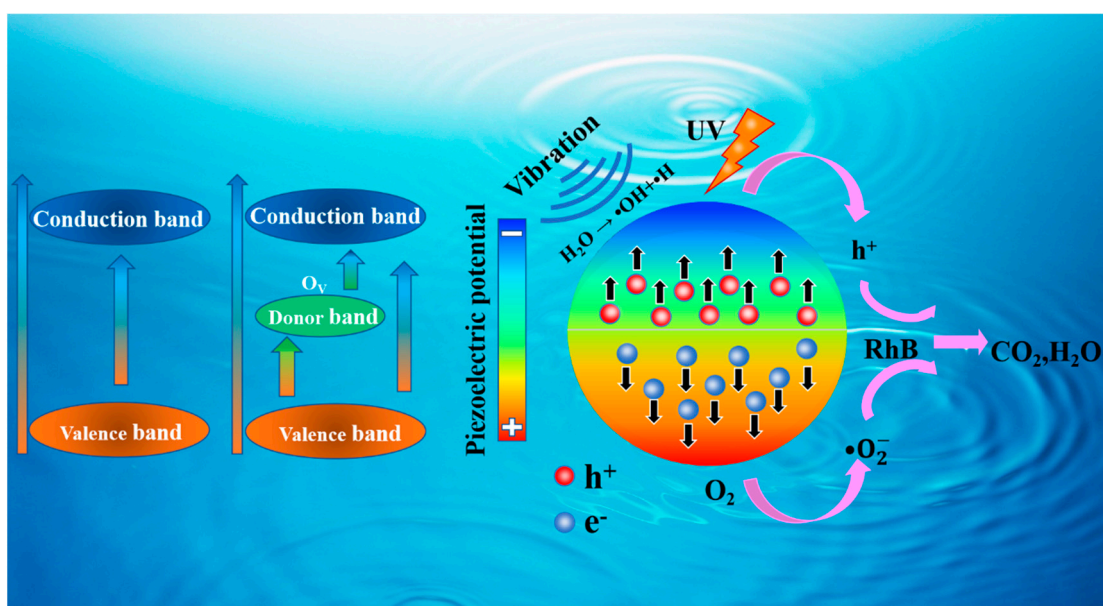


Figure 8. A schematic diagram of RhB degradation via the synergistically piezocatalytic effect of $BaTiO_3$ with oxygen vacancies.

5. Conclusions

In summary, BTO nanoparticles with varying concentrations of oxygen vacancy were synthesized by grinding BTO with lithium metal powders at room temperature. The concentration of oxygen vacancies was found to have a significant impact on the piezocatalytic performance of BTO nanoparticles. Remarkably, BTO with an optimized concentration of oxygen vacancies exhibited the highest reaction rate constant of 0.1721 min^{-1} , which is approximately four times higher than that of pristine BTO. This also demonstrates that the synergistic coupling effect of oxygen vacancies and piezoelectric catalysis-ultrasonic cavitation can generate a considerable amount of polarization charges and induce the formation of reactive superoxide radicals ($\cdot O_2^-$) and holes (h^+), which further accelerate the charge carrier separation and promote carrier transport, resulting in the enhancement of piezocatalytic efficiency. This study not only demonstrated the influence of oxygen vacancies on the piezocatalytic performance of BTO but also provided a simple and scalable method for modulating the concentration of oxygen vacancies in piezoelectric oxide catalysts at room temperature.

Supplementary Materials: The following supporting information can be downloaded at: <https://www.mdpi.com/article/10.3390/nano14030276/s1>, Figure S1. SEM images of BaTiO_{3-x} with various of Li powder treatment. (a) 0 wt%, (b) 1 wt%, (c) 3 wt%, (d) 5 wt%, (e) 7 wt%, (f) 10 wt%. The scale bar is 200 nm. Figure S2. XPS spectra (Li 1s) of lithium reduced BaTiO₃ nanoparticles. It is apparent that no peaks correspond to Li (55.5 eV) can be found in the samples, which means the generated lithium oxides have been dissolved and removed in the washing processes. Figure S3. The effect of BaTiO₃ treated with Li (wt%) on the degradation of RhB under UV irradiation without vibration. Figure S4. The absorption spectroscopy of BaTiO₃ powders treated with different Li (wt%). Their band gap has barely changed. Figure S5. (a) Cyclic stability of BTO-5. (b) XRD patterns and (c) room-temperature Raman spectra of the BTO-5 piezocatalysts before and after vibrational catalysis.

Author Contributions: Conceptualization, D.A., R.L. and S.K.; methodology, validation, D.A. and R.L.; formal analysis, investigation, D.A., R.L., H.L. (Hua Liu), C.Z., M.Y. and R.Z.; writing—original draft preparation, D.A. and S.K.; writing—review and editing, S.K.; supervision, H.L. (Han Li) and S.K. All authors have read and agreed to the published version of the manuscript.

Funding: This work was funded by the National Natural Science Foundation of China (52372104), the 2+5 project of Guangzhou University (PT252022016), and the Key Discipline of Materials Science and Engineering, Bureau of Education of Guangzhou (202255464).

Data Availability Statement: Data are contained within the article.

Acknowledgments: The authors would like to thank Shiyanjia Lab (www.shiyanjia.com, accessed on 13 May 2022) for the STEM experiments.

Conflicts of Interest: The authors declare no conflicts of interest.

References

1. Brillas, E.; Martínez-Huitle, C.A. Decontamination of wastewaters containing synthetic organic dyes by electrochemical methods. An updated review. *Appl. Catal. B Environ.* **2015**, *166–167*, 603–643. [\[CrossRef\]](#)
2. Zeng, Y.; Wu, G. Electrocatalytic H₂O₂ generation for disinfection. *Chin. J. Catal.* **2021**, *42*, 2149–2163. [\[CrossRef\]](#)
3. Wang, M.; Wang, B.; Huang, F.; Lin, Z. Enabling PIEZO potential in PIEZO electric Semiconductors for Enhanced Catalytic Activities. *Angew. Chem. Int. Ed.* **2019**, *58*, 7526–7536. [\[CrossRef\]](#)
4. Wang, Y.; Wen, X.; Jia, Y.; Huang, M.; Wang, F.; Zhang, X.; Bai, Y.; Yuan, G.; Wang, Y. Piezo-catalysis for nondestructive tooth whitening. *Nat. Commun.* **2020**, *11*, 1328. [\[CrossRef\]](#)
5. Wu, J.M.; Chang, W.E.; Chang, Y.T.; Chang, C.K. Piezo-catalytic effect on the enhancement of the ultra-high degradation activity in the dark by single- and few-layers MoS₂ nanoflowers. *Adv. Mater.* **2016**, *28*, 3718–3725. [\[CrossRef\]](#)
6. Zhang, A.; Liu, Z.; Xie, B.; Lu, J.; Guo, K.; Ke, S.; Shu, L.; Fan, H. Vibration catalysis of eco-friendly Na_{0.5}K_{0.5}NbO₃-based piezoelectric: An efficient phase boundary catalyst. *Appl. Catal. B Environ.* **2020**, *279*, 119353. [\[CrossRef\]](#)
7. Xu, S.; Hansen, B.J.; Wang, Z.L. Piezoelectric-nanowire-enabled power source for driving wireless microelectronics. *Nat. Commun.* **2010**, *1*, 93. [\[CrossRef\]](#)
8. Peng, F.; Yin, R.; Liao, Y.; Xie, X.; Sun, J.; Xia, D.; He, C. Kinetics and mechanisms of enhanced degradation of ibuprofen by piezo-catalytic activation of persulfate. *Chem. Eng. J.* **2020**, *392*, 123818. [\[CrossRef\]](#)
9. Xia, D.; Tang, Z.; Wang, Y.; Yin, R.; He, H.; Xie, X.; Sun, J.; He, C.; Wong, P.K.; Zhang, G. Piezo-catalytic persulfate activation system for water advanced disinfection: Process efficiency and inactivation mechanisms. *Chem. Eng. J.* **2020**, *400*, 125894. [\[CrossRef\]](#)
10. Wu, J.; Wang, W.; Tian, Y.; Song, C.; Qiu, H.; Xue, H. Piezotronic effect boosted photocatalytic performance of heterostructured BaTiO₃/TiO₂ nanofibers for degradation of organic pollutants. *Nano Energy* **2020**, *77*, 105122. [\[CrossRef\]](#)
11. Zhao, L.; Zhang, Y.; Wang, F.; Hu, S.; Wang, X.; Ma, B.; Liu, H.; Wang, Z.; Sang, Y. BaTiO₃ nanocrystal-mediated micro pseudo-electrochemical cells with ultrasound-driven piezotronic enhancement for polymerization. *Nano Energy* **2017**, *39*, 461–469. [\[CrossRef\]](#)
12. Wu, J.; Qin, N.; Bao, D. Effective enhancement of piezocatalytic activity of BaTiO₃ nanowires under ultrasonic vibration. *Nano Energy* **2018**, *45*, 44–51. [\[CrossRef\]](#)
13. Su, R.; Hsain, H.A.; Wu, M.; Zhang, D.; Hu, X.; Wang, Z.; Wang, X.; Li, F.-T.; Chen, X.; Zhu, L.; et al. Nano-ferroelectric for high efficiency overall water splitting under ultrasonic vibration. *Angew. Chem. Int. Ed.* **2019**, *58*, 15076–15081. [\[CrossRef\]](#)
14. Xu, X.; Jia, Y.; Xiao, L.; Wu, Z. Strong vibration-catalysis of ZnO nanorods for dye wastewater decolorization via piezo-electrochemical coupling. *Chemosphere* **2018**, *193*, 1143–1148. [\[CrossRef\]](#)
15. Yu, D.; Liu, Z.; Zhang, J.; Li, S.; Zhao, Z.; Zhu, L.; Liu, W.; Lin, Y.; Liu, H.; Zhang, Z. Enhanced catalytic performance by multi-field coupling in KNbO₃ nanostructures: Piezo-photocatalytic and ferro-photoelectrochemical effects. *Nano Energy* **2019**, *58*, 695–705. [\[CrossRef\]](#)
16. Yuan, B.; Wu, J.; Qin, N.; Lin, E.; Bao, D. Enhanced piezocatalytic performance of (Ba,Sr)TiO₃ nanowires to degrade organic pollutants. *ACS Appl. Nano Mater.* **2018**, *1*, 5119–5127. [\[CrossRef\]](#)

17. Wang, Y.-C.; Wu, J.M. Effect of controlled oxygen vacancy on H₂-production through the piezocatalysis and piezophototronics of ferroelectric R₃C ZnSnO₃ Nanowires. *Adv. Funct. Mater.* **2020**, *30*, 1907619. [[CrossRef](#)]
18. Zhang, Z.; Zou, C.; Yang, S.; Yang, Z.; Yang, Y. Ferroelectric polarization effect promoting the bulk charge separation for enhance the efficiency of photocatalytic degradation. *Chem. Eng. J.* **2021**, *410*, 128430. [[CrossRef](#)]
19. Zhu, Q.; Zhang, K.; Li, D.; Li, N.; Xu, J.; Bahnmemann, D.W.; Wang, C. Polarization-enhanced photocatalytic activity in non-centrosymmetric materials based photocatalysis: A review. *Chem. Eng. J.* **2021**, *426*, 131681. [[CrossRef](#)]
20. Lan, S.; Zeng, X.; Rather, R.A.; Lo, I.M.C. Enhanced trimethoxypyrimidine degradation by piezophotocatalysis of BaTiO₃/Ag₃PO₄ using mechanical vibration and visible light simultaneously. *Environ. Sci. Nano* **2019**, *6*, 554–564. [[CrossRef](#)]
21. Li, H.; Sang, Y.; Chang, S.; Huang, X.; Zhang, Y.; Yang, R.; Jiang, H.; Liu, H.; Wang, Z.L. Enhanced ferroelectric-nanocrystal-based hybrid photocatalysis by ultrasonic-wave-generated piezophototronic effect. *Nano Lett.* **2015**, *15*, 2372–2379. [[CrossRef](#)]
22. Xu, S.; Guo, L.; Sun, Q.; Wang, Z.L. Piezotronic effect enhanced plasmonic photocatalysis by AuNPs/BaTiO₃ heterostructures. *Adv. Funct. Mater.* **2019**, *29*, 1808737. [[CrossRef](#)]
23. Fu, J.; Yu, J.; Jiang, C.; Cheng, B. g-C₃N₄-based heterostructured photocatalysts. *Adv. Energy Mater.* **2018**, *8*, 1701503. [[CrossRef](#)]
24. Mo, S.; Li, J.; Liao, R.; Peng, P.; Li, J.; Wu, J.; Fu, M.; Liao, L.; Shen, T.; Xie, Q.; et al. Unraveling the decisive role of surface CeO₂ nanoparticles in the Pt-CeO₂/MnO₂ hetero-catalysts for boosting toluene oxidation: Synergistic effect of surface decorated and intrinsic O-vacancies. *Chem. Eng. J.* **2021**, *418*, 129399. [[CrossRef](#)]
25. Li, G.; Yang, W.; Gao, S.; Shen, Q.; Xue, J.; Chen, K.; Li, Q. Creation of rich oxygen vacancies in bismuth molybdate nanosheets to boost the photocatalytic nitrogen fixation performance under visible light illumination. *Chem. Eng. J.* **2021**, *404*, 127115. [[CrossRef](#)]
26. Wang, P.; Li, X.; Fan, S.; Chen, X.; Qin, M.; Long, D.; Tadé, M.O.; Liu, S. Impact of oxygen vacancy occupancy on piezo-catalytic activity of BaTiO₃ nanobelt. *Appl. Catal. B Environ.* **2020**, *279*, 119340. [[CrossRef](#)]
27. Mao, C.; Cheng, H.; Tian, H.; Li, H.; Xiao, W.-J.; Xu, H.; Zhao, J.; Zhang, L. Visible light driven selective oxidation of amines to imines with BiOCl: Does oxygen vacancy concentration matter? *Appl. Catal. B Environ.* **2018**, *228*, 87–96. [[CrossRef](#)]
28. Wang, S.; Hai, X.; Ding, X.; Chang, K.; Xiang, Y.; Meng, X.; Yang, Z.; Chen, H.; Ye, J. Light-switchable oxygen vacancies in ultrafine Bi₅O₇Br nanotubes for boosting solar-driven nitrogen fixation in pure water. *Adv. Mater.* **2017**, *29*, 1701774. [[CrossRef](#)]
29. Kang, Z.; Lin, E.; Qin, N.; Wu, J.; Yuan, B.; Bao, D. Effect of oxygen vacancies and crystal symmetry on piezocatalytic properties of Bi₂WO₆ ferroelectric nanosheets for wastewater decontamination. *Environ. Sci. Nano* **2021**, *8*, 1376–1388. [[CrossRef](#)]
30. Wang, P.; Li, X.; Fan, S.; Yin, Z.; Wang, L.; Tadé, M.O.; Liu, S. Piezotronic effect and oxygen vacancies boosted photocatalysis C-N coupling of benzylamine. *Nano Energy* **2021**, *83*, 105831. [[CrossRef](#)]
31. Jin, C.; Ai, J.-D.; Liu, D.-M.; Tan, L.; Cao, L.; Shen, B.; Qiu, X.; Zhang, L. Significantly enhanced piezocatalytic activity of BaTiO₃ by regulating the quenching process. *J. Mater. Chem. A* **2023**, *11*, 10360–10370. [[CrossRef](#)]
32. Ou, G.; Xu, Y.; Wen, B.; Lin, R.; Ge, B.; Tang, Y.; Liang, Y.; Yang, C.; Huang, K.; Zu, D.; et al. Tuning defects in oxides at room temperature by lithium reduction. *Nat. Commun.* **2018**, *9*, 1302. [[CrossRef](#)]
33. Freedman, D.A.; Roundy, D.; Arias, T.A. Elastic effects of vacancies in strontium titanate: Short- and long-range strain fields, elastic dipole tensors, and chemical strain. *Phys. Rev. B* **2009**, *80*, 064108. [[CrossRef](#)]
34. Herklotz, A.; Lee, D.; Guo, E.-J.; Meyer, T.L.; Petrie, J.R.; Lee, H.N. Strain coupling of oxygen non-stoichiometry in perovskite thin films. *J. Phys. Condens. Matter* **2017**, *29*, 493001. [[CrossRef](#)]
35. Madhan, K.; Jagadeeshwaran, C.; Murugaraj, R. Enhancement of electrical and magnetic properties in acceptor-doped BaTiO₃ ferroelectric ceramics. *J. Mater. Sci. Mater. Electron.* **2019**, *30*, 2953–2965. [[CrossRef](#)]
36. Joshi, U.A.; Yoon, S.; Baik, S.; Lee, J.S. Surfactant-free hydrothermal synthesis of highly tetragonal barium titanate nanowires: A structural investigation. *J. Phys. Chem. B* **2006**, *110*, 12249–12256. [[CrossRef](#)]
37. El Marssi, M.; Le Marrec, F.; Lukyanchuk, I.A.; Karkut, M.G. Ferroelectric transition in an epitaxial barium titanate thin film: Raman spectroscopy and x-ray diffraction study. *J. Appl. Phys.* **2003**, *94*, 3307–3312. [[CrossRef](#)]
38. Asiaie, R.; Zhu, W.; Akbar, S.A.; Dutta, P.K. Characterization of submicron particles of tetragonal BaTiO₃. *Chem. Mater.* **1996**, *8*, 226–234. [[CrossRef](#)]
39. Adireddy, S.; Lin, C.; Cao, B.; Zhou, W.; Caruntu, G. Solution-based growth of monodisperse cube-like BaTiO₃ colloidal nanocrystals. *Chem. Mater.* **2010**, *22*, 1946–1948. [[CrossRef](#)]
40. Jin, C.; Liu, D.; Hu, J.; Wang, Y.; Zhang, Q.; Lv, L.; Zhuge, F. The role of microstructure in piezocatalytic degradation of organic dye pollutants in wastewater. *Nano Energy* **2019**, *59*, 372–379. [[CrossRef](#)]
41. Lan, S.; Feng, J.; Xiong, Y.; Tian, S.; Liu, S.; Kong, L. Performance and mechanism of piezo-catalytic degradation of 4-Chlorophenol: Finding of effective piezo-dichlorination. *Environ. Sci. Technol.* **2017**, *51*, 6560–6569. [[CrossRef](#)] [[PubMed](#)]
42. Wu, J.; Xu, Q.; Lin, E.; Yuan, B.; Qin, N.; Thatikonda, S.K.; Bao, D. Insights into the role of ferroelectric polarization in piezocatalysis of nanocrystalline BaTiO₃. *ACS Appl. Mater. Interfaces* **2018**, *10*, 17842–17849. [[CrossRef](#)]
43. Muller, D.A.; Nakagawa, N.; Ohtomo, A.; Grazul, J.L.; Hwang, H.Y. Atomic-scale imaging of nanoengineered oxygen vacancy profiles in SrTiO₃. *Nature* **2004**, *430*, 657–661. [[CrossRef](#)] [[PubMed](#)]
44. Ding, Z.; Zhang, C.; Xu, S.; Liu, J.; Liang, C.; Chen, L.; Wang, P.; Ivey, D.G.; Deng, Y.; Wei, W. Stable heteroepitaxial interface of Li-rich layered oxide cathodes with enhanced lithium storage. *Energy Storage Mater.* **2019**, *21*, 69–76. [[CrossRef](#)]
45. Ray, S.; Kolen'ko, Y.V.; Kovnir, K.A.; Lebedev, O.I.; Turner, S.; Chakraborty, T.; Erni, R.; Watanabe, T.; Van Tendeloo, G.; Yoshimura, M.; et al. Defect controlled room temperature ferromagnetism in Co-doped barium titanate nanocrystals. *Nanotechnology* **2012**, *23*, 025702. [[CrossRef](#)]

46. Baek, K.; Lee, S.-Y.; Doh, S.-G.; Kim, M.; Hyun, J.K. Axial oxygen vacancy-regulated microwave absorption in micron-sized tetragonal BaTiO₃ particles. *J. Mater. Chem. C* **2018**, *6*, 9749–9755. [[CrossRef](#)]
47. Lin, Y.; Zhou, M.; Tai, X.; Li, H.; Han, X.; Yu, J. Analytical transmission electron microscopy for emerging advanced materials. *Matter* **2021**, *4*, 2309–2339. [[CrossRef](#)]
48. Wang, H.; Yong, D.; Chen, S.; Jiang, S.; Zhang, X.; Shao, W.; Zhang, Q.; Yan, W.; Pan, B.; Xie, Y. Oxygen-vacancy-mediated exciton dissociation in BiOBr for boosting charge-carrier-involved molecular oxygen activation. *J. Am. Chem. Soc.* **2018**, *140*, 1760–1766. [[CrossRef](#)]
49. Cai, J.; Cao, A.; Huang, J.; Jin, W.; Zhang, J.; Jiang, Z.; Li, X. Understanding oxygen vacancies in disorder-engineered surface and subsurface of CaTiO₃ nanosheets on photocatalytic hydrogen evolution. *Appl. Catal. B Environ.* **2020**, *267*, 118378. [[CrossRef](#)]
50. Elia, V.; Niccoli, M. New physico-chemical properties of water induced by mechanical treatments. A calorimetric study at 25 °C. *J. Therm. Anal. Calorim.* **2000**, *61*, 527–537. [[CrossRef](#)]
51. Hu, Y.H. A highly efficient photocatalyst—Hydrogenated black TiO₂ for the photocatalytic splitting of water. *Angew. Chem. Int. Ed.* **2012**, *51*, 12410–12412. [[CrossRef](#)]
52. Lin, T.; Yang, C.; Wang, Z.; Yin, H.; Lü, X.; Huang, F.; Lin, J.; Xie, X.; Jiang, M. Effective nonmetal incorporation in black titania with enhanced solar energy utilization. *Energy Environ. Sci.* **2014**, *7*, 967–972. [[CrossRef](#)]
53. Ning, X.; Hao, A.; Cao, Y.; Lv, N.; Jia, D. Boosting piezocatalytic performance of Ag decorated ZnO by piezo-electrochemical synergistic coupling strategy. *Appl. Surf. Sci.* **2021**, *566*, 150730. [[CrossRef](#)]
54. Yu, C.; Tan, M.; Li, Y.; Liu, C.; Yin, R.; Meng, H.; Su, Y.; Qiao, L.; Bai, Y. Ultrahigh piezocatalytic capability in eco-friendly BaTiO₃ nanosheets promoted by 2D morphology engineering. *J. Colloid Interface Sci.* **2021**, *596*, 288–296. [[CrossRef](#)]
55. Liu, D.; Jin, C.; Shan, F.; He, J.; Wang, F. Synthesizing BaTiO₃ nanostructures to explore morphological influence, kinetics, and mechanism of piezocatalytic dye degradation. *ACS Appl. Mater. Interfaces* **2020**, *12*, 17443–17451. [[CrossRef](#)]
56. Zhou, X.; Wu, S.; Li, C.; Yan, F.; Bai, H.; Shen, B.; Zeng, H.; Zhai, J. Piezophototronic effect in enhancing charge carrier separation and transfer in ZnO/BaTiO₃ heterostructures for high-efficiency catalytic oxidation. *Nano Energy* **2019**, *66*, 104127. [[CrossRef](#)]
57. Pang, Y.L.; Abdullah, A.Z.; Bhatia, S. Review on sonochemical methods in the presence of catalysts and chemical additives for treatment of organic pollutants in wastewater. *Desalination* **2011**, *277*, 1–14. [[CrossRef](#)]
58. Starr, M.B.; Wang, X. Fundamental analysis of piezocatalysis process on the surfaces of strained piezoelectric materials. *Sci. Rep.* **2013**, *3*, 2160. [[CrossRef](#)]

Disclaimer/Publisher's Note: The statements, opinions and data contained in all publications are solely those of the individual author(s) and contributor(s) and not of MDPI and/or the editor(s). MDPI and/or the editor(s) disclaim responsibility for any injury to people or property resulting from any ideas, methods, instructions or products referred to in the content.